IOP PUBLISHING JOURNAL OF PHYSICS: CONDENSED MATTER

J. Phys.: Condens. Matter **21** (2009) 035116 (12pp) doi:10.1088/0953-8984/21/3/035116

Theory of the low frequency mechanical modes and Raman spectra of the M13 bacteriophage capsid with atomic detail

Eric C Dykeman and Otto F Sankey

Department of Physics, Center for Biological Physics, Arizona State University, Tempe, AZ 85287-1504, USA

Received 20 August 2008, in final form 13 November 2008
Published 15 December 2008
Online at stacks.iop.org/JPhysCM/21/035116

Abstract

We present a theoretical study of the *low* frequency vibrational modes of the M13 bacteriophage using a fully atomistic model. Using ideas from electronic structure theory, the few lowest vibrational modes of the M13 bacteriophage are determined using classical harmonic analysis. The relative Raman intensity is estimated for each of the mechanical modes using a bond polarizability model. Comparison of the atomic mechanical modes calculated here with modes derived from elastic continuum theory shows that a much richer spectrum emerges from an atomistic picture.

(Some figures in this article are in colour only in the electronic version)

1. Introduction

Viruses are the smallest of living organisms. The designation 'living' is often debated since they do not have even a single cell. However, they possess genetic material and have the ability to reproduce, but only by attacking a host cell. This makes them a form of obligate intracellular parasite—an exploitative parasite that takes over the protein and genomic replication machinery of their hosts to reproduce and survive.

Viruses present a persistent threat to all living organisms. Viruses attack humans, plants, animals and bacteria. They cause a multitude of diseases in humans, and are a threat to agriculture invading both livestock and cultivated plants. Vaccines are an effective method to protect against viral attack if a suitable vaccine for a specific virus can be developed. Treatment after a virus has infected its host is particularly difficult. There are no known broad spectrum antiviral drugs—since viruses use much of the host's protein machinery to reproduce, attacking this machinery attacks the host. Thus drug therapies are often dangerous since they may produce side effects making them unsuitable for treatments over long times. A further difficulty in attacking viral infections is the rapid rate of mutations of the virus. Often drugs or vaccines quickly loose their effectiveness as mutations of the virus make them ineffective.

Bacteriophages are viruses that attack prokaryotes. Phages have developed ingenious strategies to survive and are enormously diversified in their structure. This leads to a diversity of means to attack and exploit their hosts. Some phage structures are richly complex, with the most numerous morphology being the tailed phages. Tailed phages have an icosahedral head capsid attached to a collar and neck with a contractile sheath covering a long core. At the base of the core are long fibrous spider-like legs. Well known among this group are the T4, λ, and $\phi 29$. Less complex are the filamentous bacteriophages in which M13, the subject of this work, is an example.

This paper is concerned with the vibrational properties of the M13 virus. Why is there interest in the vibrational properties of biological systems and in viruses in particular? There are several reasons and we list three. The first relates to the rather unique properties of M13. Tubular viral structures such as M13 or the larger diameter tobacco mosaic virus (TMV), are being developed as templates to assemble nanostructures [1–5] such as to produce uniform semiconductor nanoparticles or metallic nanowires. Component size resulting in the nanoparticle synthesis is difficult to control and nanostructures templated from viral capsids present opportunities to create more uniform structures. Raman scattering and vibrational mode analysis is a non-destructive method to monitor the assembly process. Extensive contact of a fibrous virus capsid with long wires or semiconducting threads will alter the low frequency modes of the virus thus producing a non-invasive means to monitor

nanoparticle synthesis. The nanotechnological properties of filamentous bacteriophage M13 recently led to single molecule studies of their stretching properties in an optical trap [6].

A second reason to investigate mechanical modes is that viruses are pathogens and their vibrational properties potentially can be used to combat viral infections. There has been a recent suggestion [7] that viruses can be damaged up by exciting their vibrations. Tsen and co-workers [8–11] have shown that inelastic light scattering with a pulsed laser [12] may provide an effective means to destroy viruses by resonantly exciting mechanical vibrations. As such, an atomic level description of the displacement patterns becomes essential in order to understand the coupling of the mechanical modes to external probes such as light.

The third reason for studying vibrational modes is a general one. Protein assemblies and biomolecules have enzymatic activity that is connected to the floppy or hinged motions of the assembly. The large scale conformational motions of the assembly have their genesis in the very low frequency modes. Specifically, for viruses a conformational changes in the viral capsid is often necessary for the release and injection of the genomic material into the host. This area of research is still emerging, but good examples of the importance of this effect have been identified, such as the structural transition of the poliovirus upon interaction with a host cell receptor [13], or a pucker-like mode about a C5-axis of the icosahedral human rhinovirus to inject its RNA into the cell cytoplasm [14]. Additionally, normal mode analysis (NMA) is used to model enzyme specificity [15] and its changes due to mutations, as well as in B-factor analysis of x-ray structures. Normal mode analysis offers an alternative method to molecular dynamics (MD) to study the configurations within a single local energy minimum configuration.

In this paper, we present a method based on order N techniques from electronic structure theory to determine the low frequency normal modes and frequencies of large ($>10^4$ atoms) systems using a fully atomistic classical force field model and a *full* basis set. A full basis set means that the vibrational modes are constructed from the individual atomic displacements (3 for each atom in the system) and hence is complete. The theoretical method extends previous work on an icosahedral virus [16]. We model the M13 bacteriophage as an infinitely long molecule and use periodic boundary conditions for a single unit cell of bacteriophage which is 161.5 Å in length. First, we briefly review the order N method used in electronic band-structure calculations. Next, we apply these ideas from electronic systems to the problem of finding the low frequency phonons of a classical dynamical matrix. Then we apply the method to determine the low frequency mechanical mode patterns and frequencies of the M13 bacteriophage capsid, a cylindrical virus whose capsid is composed of many alpha helical protein segments. The relative Raman intensity for each mode is then predicted using a bond polarizability model. Finally, the fully atomistic modes are compared with previous studies of the M13 bacteriophage which used continuum elastic theory to predict the frequency and displacement patterns of its capsid.

2. Preliminaries

The 'standard' route for NMA involves the harmonic approximation where the potential energy of the molecule is Taylor expanded to second order about equilibrium in terms of the displacements $\vec{u}_i$ of each atom i. The classical equations of motion result in a matrix equation for the displacement pattern $\mathbf{u}$ for each normal mode of frequency ω,

$$\overleftrightarrow{\Phi}\,\mathbf{u} = \omega^2\,\overleftrightarrow{M}\,\mathbf{u}, \tag{1}$$

where the matrices $\overleftrightarrow{\Phi}$ and $\overleftrightarrow{M}$ are the force constant matrix (Hessian) and the diagonal mass matrix respectively. The matrix elements are given by

$$\Phi_{ij} = \frac{\partial^2 V}{\partial u_{i\alpha}\,\partial u_{j\beta}}, \qquad M_{ij} = m_i\delta_{ij}. \tag{2}$$

The force constant matrix elements are second derivatives of the total potential energy V of the molecule with respect to displacements of atoms i and j in the αth and βth directions respectively.

The potential energy model we use is empirical. The second derivatives Φ_{ij} are computed analytically, in the same spirit as analytic forces are computed in MD. More details on this will be described in the appendix. The potential energy contains five contributions—they are due to bond stretching, bond angle distortions, dihedral energy contributions (4-atom terms), Coulomb interactions, and van der Waals interactions. The parameters for these interactions are obtained from the AMBER force field model [17]. While the AMBER force field has parameters for water molecules, explicit water is not included in our model. Instead, water is implicitly included in the parameter set using the generalized Born (GB) model [18, 19]. This is especially important for the Coulomb interactions which include solvation effects and an environment dependent dielectric screening. The GB model uses a finite range for the Coulomb interactions and a 10 Å cutoff is presently used. Thus only a direct summation is used to evaluate Coulomb effects and Ewald summation methods are not used even though periodicity exists. The chosen cutoff results in screened Coulomb interactions that only extend slightly into a single neighboring cell.

Diagonalizing the matrix equation (equation (1)) provides a complete set of normal mode frequencies and atomic displacement patterns of the molecule. However, as the number of atoms in the molecule increases, diagonalization becomes impossible. Two problems due to the large size are that (i) the amount of computer memory required to store the force constant matrix elements for molecules with $N > 10^4$ atoms is often several Tb (10^{12} bytes) and (ii) the time required to diagonalize equation (1) scales as the number of atoms cubed. Direct diagonalization of the force constant matrix can be performed on small systems (roughly on the order of a few thousand atoms). For example, this is the approach taken by Miller *et al* [15] to study the change of normal mode displacement patterns due to mutations in α-Lytic protease. However, large proteins and protein complexes with tens or hundreds of thousands of atoms (like viruses) are out of reach

with direct diagonalization methods. Hence, an alternate method is necessary, and it must not require storage of the force constant matrix.

Two paths can be taken. One is to simplify the problem by physical approximations. The other is to maintain the full problem but develop methodologies to make the problem tractable. We first mention often used approaches that use physical approximations. Much prior normal mode analysis of large proteins or macromolecular structures has relied on continuum elastic theory (CET) [11, 20, 21], the elastic network model (ENM) [22, 23], or the rotation translation block method (RTB) [24, 25]. These methods coarse grain [26] the molecule (i.e. use a reduced basis set to construct the vibrational modes) so that a normal mode analysis is possible. Using a reduced set of coordinates is also often done to simplify the problem. For example, dihedral and torsional distortions have smaller restoring forces than bond or angle stretching forces. Thus dihedral and torsional distortions play a larger role in the low frequency oscillations, and thus the problem is simplified by including just these degrees of freedom. Using only rotational degrees of freedom through torsional generalized coordinates has been used to study the dynamic character of human blood coagulation factor and human tissue factor [27].

A second path to study mechanical motions of large structures is to maintain the atomistics of the problem but use a methodology that allows at least part of the problem to be solved. The method used and developed in this paper falls into this category. Specifically only the low frequency modes are determined by a functional minimization algorithm. Other methods exist which have similar goals but use quite different strategies. A review of some of these methods is given by Hayward [28], and the most widely used method is the Lanczos recursion method [29]. This method repeatedly applies the dynamical matrix to a vector and it quickly amplifies the eigenvectors corresponding to the extreme eigenvalues. Block recursion can be used to iterate within a subspace. The method must be used with extreme caution because the repeated multiplication has instabilities and can produces 'ghosts' and 'clones' [30] which repeat multiple copies of a vector. In a full atomistic calculation of a large biomolecule, ω may vary from 0.4 to 4000 cm^{-1}, which means the ratio of the largest to the smallest eigenvalue λ ($=\omega^2$) is of order $10\,000^2 = 10^8$. This makes for an ill-conditioned matrix that is particularly sensitive to numerical round off. We have found that as a result, the *lowest* eigenvalues are difficult to find using Lanczos schemes. Nevertheless, this method has enjoyed success.

Normal mode analysis has its limitations. It is easy to generate a long list of deficiencies, and we mention some of the prime difficulties. First, normal mode models assume that the biomolecule is trapped into a single minimum free energy configuration. True biological molecules are often sampling multiple configurations and hopping from one to another. Second, normal mode analysis assumes that the single configuration is harmonic about its minimum. Third, damping due to anharmonic effects or from the solvent are not included. And finally, to perform a normal mode analysis, the structure of the biomolecule must be known, which is not always the case. Normal mode analysis however gives a simple, yet restricted, picture of at least the motions in one local minimum energy configuration, and offers a starting point from which advancements can be attained. For example, the effect of damping can (at least in principle) be included by generalizing the normal mode concept to a Langevin mode analysis which includes a friction matrix [31].

3. Order *N* method for electronic structure calculations

In this section we briefly discuss order-N methods within the context of electronic structure. This sets the stage for section 4 where we generalize the method for application to mechanical vibrations. The method has been described in abbreviated form in an earlier publication [16]. In electronic structure calculations of a molecule or crystal, one desires the electronic wavefunctions from the set of *lowest* energy orbitals ψ_i. These orbitals are eigenfunctions of a Schrödinger equation, $\hat{H}\psi_i = \lambda_i\psi_i$, where λ_i is the single particle energy of the state ψ_i. The total energy has many contributions, but the computationally difficult contribution to determine is the 'band-structure' energy G, where G is the sum of single particle energies over the occupied orbitals,

$$G = \sum_{i(\text{occupied})} \lambda_i. \tag{3}$$

This assumes a gap between occupied and unoccupied levels (i.e. an insulator or semiconductor). To perform the sum, the eigenvalues must be known which requires solution of the Schrödinger equation (assumed here to be a matrix equation of large dimension). The matrix is assumed to be too large to diagonalize directly. However, G requires only a subset of eigenvalues (those corresponding to the occupied states); thus diagonalization of the full matrix gives far more information than needed. Thus an alternative scheme is used which leads to minimization of an energy functional for G that gives precisely the same result as equation (3).

The beginning concept is to rewrite G using properties of a Trace and the Fermi–Dirac operator as

$$G = \mathrm{Tr}(\hat{f}\hat{H}), \tag{4}$$

where Tr denotes the trace and $\hat{f}$ is the Fermi–Dirac operator

$$\hat{f}(\hat{H},\mu) = \frac{1}{e^{\beta(\hat{H}-\mu)}+1}. \tag{5}$$

We assume the low temperature insulating regime where the chemical potential μ lies within the bandgap, so that eigenstates ψ_i are either 'occupied' ($\lambda_i < \mu$) or 'unoccupied' ($\lambda_i > \mu$). Thus

$$\begin{aligned} \hat{f}(\hat{H},\mu)\psi_i &= 1\times\psi_i \qquad \text{if } \lambda_i < \mu \\ \hat{f}(\hat{H},\mu)\psi_i &= 0\times\psi_i \qquad \text{if } \lambda_i > \mu. \end{aligned} \tag{6}$$

The trace in equation (4) can be performed over *any* complete orthonormal basis set of states. Since the unoccupied

states do not contribute to G, using any orthonormal basis ϕ_i that spans the occupied states to compute the trace in equation (4) leads to exactly equation (3).

In light of the above arguments, a functional minimization can be introduced over a *smaller* set of M *occupied* states which are varied (V),

$$G_{\mathrm{V}} = \mathrm{Min}[\mathrm{Tr}_M(H)]. \tag{7}$$

The M states are varied so as to minimize G. Since the trace extends over only M states, the storage of state vectors is greatly reduced. However, the minimum of G_{V} occurs when all electrons drop down into a lowest level with eigenvalue λ_0, i.e. the M states become just one state repeated M times. The functional G_{V} (equation (7)) is ignorant of the Pauli exclusion principal and of orthogonality of the state spectrum of single particle levels.

This is a severe obstacle which made such approaches of little use. In the early to mid 90s several so-called order-N breakthroughs occurred that solved this problem. There are now many ways to proceed [32–35], and deep connections exist amongst the many ways. For example the method of Nunes *et al* focused on idempotency of the density matrix—idempotency in the eigenfunction representation is tantamount to having N occupied states that are orthonormal. We use the Ordejon, Drabold, Martin and Grumbach (ODMG) [32] functional minimization that enforces the orthogonality and the exclusion principal. The ODMG is deceptively simple and is

$$G_{\mathrm{V}} = \mathrm{Min}[\mathrm{Tr}_M(H + H(1 - S))]. \tag{8}$$

The trace is over the $M \times M$ matrices H and S formed with M vectors ϕ_i. The overlap matrix S has elements given by $S_{ij} = \langle\phi_i|\phi_j\rangle$. The vectors ϕ_i are varied as part of the minimization procedure, and once minimized, the M vectors form an orthogonal set that span the space of the M *lowest* energy states of $\hat{H}$. The value of G_{V} at the minimum (and nowhere else) is precisely the value of equation (4).

That such a simple function gives the exact result is somewhat surprising. To see how it works, let us consider a Hamiltonian with a single normalized state ψ_0 with energy $-\lambda_0$. Then the single state ψ_0 is an eigenstate of $\hat{H}$. We choose a vector ϕ to perform the trace, and since the problem is a (trivial) one-dimension problem, ϕ can only be proportional to ψ_0, which we write as $|\phi\rangle = \sqrt{(}S)|\psi\rangle$. The parameter S is varied in order to minimize G_{V}. The matrix elements are $S = \langle\phi|\phi\rangle$ and $H = \langle\phi|\hat{H}|\phi\rangle = -S\lambda_0$ which yields $G_{\mathrm{V}} = \mathrm{Min}[-S\lambda_0 + S\lambda_0(1 - S)]$. The expression for G_{V} can be manipulated to $G_{\mathrm{V}} = -\lambda_0 + \lambda_0(1 - S)^2$. Figure 1 shows G_{V} (equation (8)) and the various contributions. Also shown is $\mathrm{Tr}(H) = -\lambda_0 S$. Clearly $\mathrm{Tr}(H)$ has no minimum. The effect of the ODMG functional is to add a 'harmonic potential' $\lambda_0(1 - S)^2$ to $-\lambda_0$. This produces a minimum energy for G_{V} at the correct result $-\lambda_0$ and at the properly normalized state $\langle\phi|\phi\rangle = S = 1$.

One notes that if the eigenvalue $-\lambda_0$ were instead $+\lambda_0$, the curvature of the harmonic potential changes sign and instead of a minimum at the correct value of $S = 1$, G_{V} has a maximum value. This is a limitation of the method— H must have a completely negative spectrum in order to produce a minimum. We will deal with this complication in section 4 for the vibrational problem which has a positive definite spectrum for a stable system.

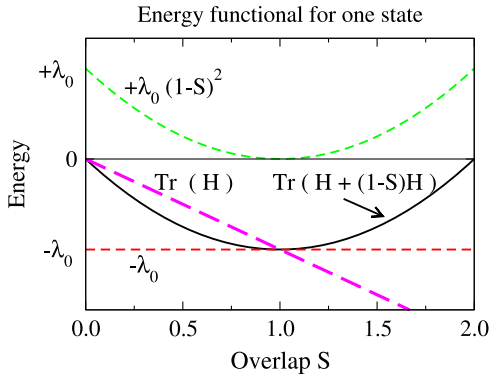

Figure 1. A plot of the ODMG energy functional (G_{V}) as a function of the overlap S for a Hamiltonian matrix of one dimension with single eigenvalue $-\lambda_0$. The overlap S is the single variational parameter. The two contributions to G_{V} are shown ($-\lambda_0$ and $+\lambda_0(1 - S)^2$). The sum of these two is $G_{\mathrm{V}} = \mathrm{Tr}(H + (1 - S)H)$ is also shown. Note that effectively there is a harmonic potential which acts to drive the system toward the correct normalized state ($S = 1$) with correct energy $-\lambda_0$. The simpler energy functional $\mathrm{Tr}(H)$ for this one-dimensional illustratory example is $-\lambda_0 S$, which has no minimum.

4. Functional for the low frequency vibrations

In biomolecular complexes such as viruses, the low frequency vibrations (e.g. <25 cm^{-1}) are of most interest since low frequency modes characterize either the 'floppy' regions or relate to global motions of large regions within the complex. Large global motions are likely to be involved in breaking apart the virus during resonant excitations from external probes. A large biomolecular system has many high frequency deformations while the desired low frequency motions are much less numerous. This is the viewpoint taken in the present study. Our primary motivation is to seek low frequency motions that are targets to excite for inactivation of a virus.

To determine the low frequency modes, we make an analogy between the low frequency phonon problem and the electronic structure problem. We consider the wanted low frequency phonon states to be a set of 'occupied' states in the spectrum and the high frequency states to be an 'unoccupied' set. This has the effect of introducing a pseudo-Fermi level in the vibrational frequencies ω_{F}. Figure 2 illustrates the basic idea where the lowest M states of the phonon spectrum are 'occupied' while all other states are 'unoccupied'. Essentially, we treat phonons as fermions (from a purely mathematical perspective) making the problem mathematically identical to the electronic structure problem. This is strictly a device to obtain the sub-spectrum of a matrix (here the dynamical matrix, and for the electronic structure problem the Hamiltonian matrix). Once the sub-spectrum is obtained, the improper statistics are never used to incorrectly compute a physical quantity.

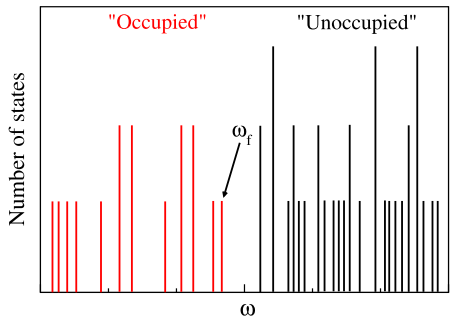

Figure 2. A schematic number of states as a function of frequency ω. States below a pseudo-Fermi level ω_F act as occupied states in the algorithm, and states above are unoccupied. Upon convergence, the functional minimization of G_p produces the eigenvectors and frequencies ω of the dynamical matrix for all 'occupied' levels.

We now introduce the phonon (p) energy functional as

$$G_p = \mathrm{Min}[\mathrm{Tr}_M(H + H(1 - S))]. \tag{9}$$

The 'Hamiltonian' matrix H and the overlap matrix S are *small* $M \times M$ matrices with elements defined in terms of the dynamical matrix $\overleftrightarrow{D}$ and the variational vectors $|u\rangle$

$$\begin{aligned} H_{ij} &= \langle u_i|\hat{D}_s|u_j\rangle \\ S_{ij} &= \langle u_i|u_j\rangle. \end{aligned} \tag{10}$$

The operator $\hat{D}_s$ is the shifted dynamical matrix operator $\hat{D}_s = \hat{D} - \lambda_L\hat{I}$, where λ_L is the largest eigenvalue of $\hat{D}$. The purpose of the shift is to produce a negative definite spectrum which guarantees an energy minimum in the ODMG energy functional [32], and hence in G_p. As was seen in our example illustration in figure 1, a minimum is produced when the eigenvalue is negative and a maximum produced when it is positive. The shift leaves the eigenvectors unaffected. The largest eigenvalue λ_L is quite easy to find. The Lanczos recursion iteration technique rapidly converges to produce λ_L, especially since the ratio between the lowest (non-zero) eigenvalue and the largest is of order 10^8. Usually less than ten recursion iterations are needed for convergence. As a precaution, a small safety buffer of a couple percent is added to λ_L.

The search for the M lowest frequency modes of $\hat{D}$ begins by choosing a random set of M vectors $|u_i\rangle$ ($i = [1, M]$) that need not be orthogonal or even normalized. The functional G_p upon iteration will automatically enforce orthonormality. The phonon energy functional (equation (9)) is then minimized. The phonon functional G_p is a function of $3N \times M$ variables (M vectors times $3N$ components). Despite the size of the minimization space, the minimization procedure proceeds quickly since there is an infinity of solutions—*any* set of orthonormal vectors that span the subspace of the M lowest states $\hat{D}$ is a solution. This produces a wide target.

After minimization is completed, the vectors $|u_i\rangle$ are an orthonormal set of vectors that span the space of the *lowest* M states of $\hat{D}$. The vectors $|u_i\rangle$ are not eigenvectors of $\hat{D}$. The true eigenvectors ($|e_i\rangle$) are obtained from a diagonalization of the small $M \times M$ matrix equation

$$HC(i) = \lambda' SC(i). \tag{11}$$

The overlap matrix S will be the identity matrix at the exact minimum; since computational convergence is never perfect, including the computed overlap S at this step partially corrects errors.

The eigenvalues λ' are shifted from the true eigenvalues of $\hat{D}$ via $\lambda' = \lambda - \lambda_L$. The vector $C(i)$ of length M gives the linear combination of basis vectors $|u\rangle$ that produce the eigenvector $|e_i\rangle$ i.e.

$$|e_i\rangle = \sum_{j=1}^{M} C_j(i)|u_j\rangle. \tag{12}$$

5. Minimization of the phonon functional G_p

Any minimization scheme can be used to minimize the phonon energy functional G_p (equation (9)). Here we describe the use of a conjugate gradient method (CG), which we found to work well. There are many forms of CG that seek to optimize convergence. We use the method of Pollak and Ribiere [36] which converges better than the traditional Fletcher–Reeves method. An important practical feature of a CG minimization of the G_p functional is that the line minimization needed to perform a conjugate gradient step is done *analytically* (described below). This is quite fortunate since it eliminates much of the computational expense of the CG algorithm.

Consider the kth current vector at the nth iteration to be $|u_k^n\rangle$ and the CG search direction vector for a new minimum to be along $|p_k^n\rangle$. The gradient of G_p is needed in the construction of the search direction vector. The gradient $|g_k^n\rangle$ of the vector $|u_k^n\rangle$ at step n is obtained by differentiating equation (9) with respect to the current state $|u_k^n\rangle$,

$$\begin{aligned} |g_k^n\rangle &= 4\hat{D}_s|u_k^n\rangle + 2\sum_i \hat{D}_s|u_i^n\rangle\langle u_i^n|u_k^n\rangle \\ &\quad + 2\sum_i |u_i^n\rangle\langle u_i^n|\hat{D}_s|u_k^n\rangle. \end{aligned} \tag{13}$$

The gradient is used to form the CG search direction vector

$$|p_i^n\rangle = -|g_i^n\rangle + \beta^n|p_i^{n-1}\rangle. \tag{14}$$

In CG, β^n is determined by taking a ratio of the magnitudes of new and old gradients. For a standard function of s variables, the gradient will have a total of s components. The phonon energy functional G_p has a gradient of $3N \times M$ components that are given by the M individual gradient vectors of length $3N$ for each state vector (equation (13)). Thus, the Pollak and Ribiere CG constant [36] β^n is given by

$$\beta^n = \frac{\sum_i[\langle g_i^n|g_i^n\rangle - \langle g_i^n|g_i^{n-1}\rangle]}{\sum_i\langle g_i^{n-1}|g_i^{n-1}\rangle}. \tag{15}$$

The line minimization is achieved by updating all vectors by taking the same step size γ^n. Thus

$$|u_i^{n+1}\rangle = |u_i^n\rangle + \gamma^n|p_i^n\rangle. \tag{16}$$

For a general function of s variables, an extremum will occur at a point along a search direction if and only if the gradient vector of the function with s components is perpendicular to the search direction at that point. Thus, in order for the phonon energy functional G_{p} with $3N \times M$ variables to be minimized,

$$\sum_i \langle g_i^{n+1} | p_i^n \rangle = 0 \tag{17}$$

must be satisfied.

Equation (16) can be substituted into equation (13) to form the gradient at step $n+1$. Then taking the dot product with the search directions and summing over all vectors, the orthogonality condition (equation (17)) yields a cubic equation in terms of the step γ^n

$$A(\gamma^n)^3 + B(\gamma^n)^2 + C(\gamma^n) + D = 0, \tag{18}$$

where the coefficients A–D are defined as (using an Einstein summation convention)

$$\begin{aligned}
A &= 4\langle p_i^n | p_j^n \rangle \langle p_j^n | \hat{D}_{\mathrm{s}} | p_i^n \rangle \\
B &= 3\langle p_i^n | \hat{D}_{\mathrm{s}} | p_j^n \rangle \left(\langle p_j^n | u_i^n \rangle + \langle u_j^n | p_i^n \rangle \right) \\
&\quad + 3\langle p_i^n | p_j^n \rangle \left(\langle p_j^n | \hat{D}_{\mathrm{s}} | u_i^n \rangle + \langle u_j^n | \hat{D}_{\mathrm{s}} | p_i^n \rangle \right) \\
C &= -4\langle p_i^n | \hat{D}_{\mathrm{s}} | p_i^n \rangle + 2\left(\langle p_i^n | \hat{D}_{\mathrm{s}} | u_j^n \rangle + \langle u_i^n | \hat{D}_{\mathrm{s}} | p_j^n \rangle \right) \\
&\quad \times \left(\langle p_j^n | u_i^n \rangle + \langle u_j^n | p_i^n \rangle \right) \\
&\quad + 2\langle p_i^n | \hat{D}_{\mathrm{s}} | p_j^n \rangle \langle u_j^n | u_i^n \rangle + 2\langle u_i^n | \hat{D}_{\mathrm{s}} | u_j^n \rangle \langle p_j^n | p_i^n \rangle \\
D &= -4\langle p_i^n | \hat{D}_{\mathrm{s}} | u_i^n \rangle + \langle u_i^n | \hat{D}_{\mathrm{s}} | u_j^n \rangle \left(\langle p_j^n | u_i^n \rangle + \langle u_j^n | p_i^n \rangle \right) \\
&\quad + \langle u_i^n | u_j^n \rangle \left(\langle p_j^n | \hat{D}_{\mathrm{s}} | u_i^n \rangle + \langle u_j^n | \hat{D}_{\mathrm{s}} | p_i^n \rangle \right).
\end{aligned} \tag{19}$$

The solution to the cubic equation produces two possibilities for the roots: (i) one real and two complex roots, or (ii) three real roots. In case (ii), the root which most deeply minimizes the G_{p} functional is selected. Once the step size γ^n has been obtained, the vectors $|u_i^n\rangle$ are updated using equation (16). The dynamical matrix operating on the vectors $|u_i^n\rangle$ can also be updated

$$\hat{D}_{\mathrm{s}} | u_i^{n+1} \rangle = \hat{D}_{\mathrm{s}} | u_i^n \rangle + \gamma^n \hat{D}_{\mathrm{s}} | p_i^n \rangle. \tag{20}$$

Each step of the minimization procedure of G_{p} will require M dynamical matrix operations on a vector—one necessary for the update of each $|u_i\rangle$. Although the time to minimize the phonon functional is likely to have a complicated dependence on M and N, some estimates can be made. Since the dynamical matrix operating on each vector can be computed in order N steps (see appendix), a very simple approximation is that the time for minimization of the phonon functional scales roughly as order MN.

The total number of vectors of length $3N$ that must be stored for the CG procedure is $5M$. Since the density of states is small at low frequencies, $M = 100-200$ is usually sufficient to reach 30 cm^{-1} when $N = 10^4$ with a memory requirement of roughly 114 MB (double precision). The calculations reported in section 6 are performed with one processor on a unix PC.

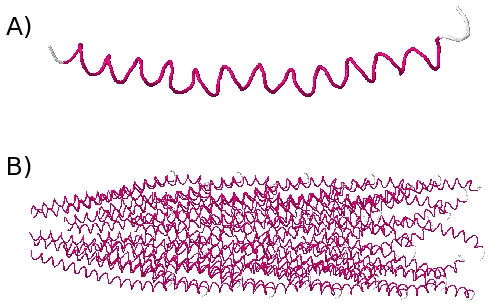

Figure 3. The structure of the M13 tubular vial capsid. (a) A single α-helix building block protein. (b) The single α-helix proteins are arranged in a tubular (helical symmetry) fashion on the outer surface of a cylinder. The system is periodic and the segment shown, which contains 50 single α-helix building block proteins, is one full period which has a length of roughly 16 nm.

6. Low frequency modes of M13 phage

M13 is a filamentous bacteriophage with a circular single stranded DNA genome of approximately 6400 nucleotides. The virus belongs to the viral family Inoviridae. The virus has no envelope and is a model system to study the properties of viruses. It is often used in biological modeling because of its small genome which codes for only about ten proteins. The structure of the M13 bacteriophage capsid is a long, hollow cylindrical tube composed of α-helix building units, as shown in figure 3(a), arranged on a tubular surface. A single α-helix is composed of 50 amino acids and has a total of 741 atoms. The full capsid structure is built using multiple copies of the α-helix building block arranged using helical symmetry. The final full capsid structure has a length and diameter of roughly 800 nm and 6 nm respectively.

Since the full capsid structure is composed of repeating α-helix building blocks, the structure is periodic and can be treated as a long (infinite) tube with a unit cell. A single periodic unit is illustrated in figure 3(b). The periodic unit is composed of 50 α-helix building blocks that form a segment of the capsid that has a length of approximately 16 nm with a total of 37 050 atoms (including hydrogen).

Coordinates for the single alpha helix building block (figure 3(a)) were obtained from the protein data bank (PDB code 2C0W). The 2C0W structure was determined from x-ray crystallography [37]. The 2C0W coordinates were used to construct a periodic segment of the full tubular capsid by assembling 50 copies using the rotation matrices provided in the PDB file. This created a periodic unit where the tube axis was aligned with the z-axis. Periodic boundary conditions were used. The system is made to have artificial periodicity in the lateral x and y directions by inserting replicas of the central tube. The lateral lattice vectors were made large enough so that there were no interactions with nearest neighboring tubes in the x and y directions.

The 37 050 atoms in the periodic unit were minimized using the AMBER 94 [17] force field with generalized Born Coulomb interactions [18, 19, 38] in the molecular dynamics program suite *Saguaro* [39]. A 10 Å cutoff was used for both the generalized Born and van der Waals interactions. The RMS

gradient of the final optimized structure was <0.001 eV Å^{-1} and produced an RMSD from the x-ray structure of 1.61 Å. This minimization procedure is constant with other work [40] where the goal of minimization is to keep the structure within about 1 Å of its x-ray structure. Since the final RMS gradient was not zero to machine precision, negative eigenvalues $\lambda = \omega^2 < 0$ can occur. A total of 49 negative eigenvalue states were found. An examination of the negative eigenvalue states that appeared in our calculation showed that their eigenvectors were highly localized on a few atoms (<100) and their frequency was small in magnitude (<20 cm^{-1}). For example, one negative mode had displacements located on the last amino acid of a single α-helix building unit. The other negative modes are similar to this. Thus these modes correspond to 'dangling' regions. As such, they are ignored in what follows.

The phonon energy functional G_p (equation (9)) was CG minimized for $M = 200$ vectors using the analytical cubic equation scheme described above. The optimized coordinates of M13 were used to calculate the operation of the dynamical matrix on a vector using a 10 Å cutoff for the electrostatic and van der Waals interactions (see appendix for details of the procedure). The length of each vector, which is the dimensions of the space for a single unit cell, is 111 150 ($3N = 3 \times 37\,050$). Approximately 4000 CG steps were performed which required a total of roughly 8×10^5 dynamical matrix operations on a vector. The computational cost can be thought of as approximately 8×10^5 MD steps on 37 050 atoms.

Since minimization on a computer rarely achieves a zero gradient, we calculated the residual 'error' vector ($|r\rangle = \hat{D}|e^*\rangle - \lambda^*|e^*\rangle$) for each of the low frequency modes of M13. The vector $|e^*\rangle$ is the approximate eigenvector calculated with equation (11) and λ^* is the approximate eigenvalue given by $\lambda^* = \langle e^*|\hat{D}|e^*\rangle$. The magnitude of the residual vectors were approximately $|r| \approx 10^{-4}$ for all of the low frequency modes of M13 calculated with the phonon energy functional. Tests on other smaller molecules such as ubiquitin have shown that eigenvectors with residuals of this magnitude have errors in the frequencies on the order of 0.01cm^{-1}.

Continuum theory [11] predicts four basic types of mode displacement patterns for a tubular virus—radial, torsional, radial-torsional, and axial. The atomistic modes of M13 however will have some amount of displacement along each of the cylindrical unit vector directions. This is due to the atomistic structure of the capsid which tends not to permit pure radial, torsional, or axial motion. Nevertheless, the atomistic modes can also be separated into one of these four categories based on the direction of a majority of the displacement pattern. Table 1 lists the 30 lowest frequencies of the M13 phage and its mode type, as well as the participation number (W_λ). The participation number for the mode gives a measure for how localized or extended the displacement pattern is. The participation number W_λ is defined as

$$W_\lambda = e^{S_\lambda}, \tag{21}$$

where S_λ is the (information) entropy of the mode given by

$$S_\lambda = -\sum p_i(\lambda) \ln [p_i(\lambda)]. \tag{22}$$

Table 1. Frequencies (ω_i in cm^{-1}) and participation numbers W_i for the 30 lowest modes of the M13 bacteriophage capsid. Full participation is 37 050. Each mode is given a corresponding type of radial (R), axial (A), torsional (T), or radial-torsional (RT) based on direction of a majority of the displacement pattern (>50%).

Type	ω_i	W_i	Type	ω_i	W_i
RT	1.45	10 616	RT	3.57	23 408
RT	1.62	30 496	RT	3.60	17 527
RT	1.74	34 123	RT	3.65	22 527
RT	1.89	26 039	RT	3.72	19 154
RT	2.20	6 690	RT	3.80	25 295
RT	2.49	4 224	RT	3.82	23 583
T	2.67	24 955	RT	3.88	22 497
T	2.72	21 293	A	3.97	23 500
RT	3.15	18 103	A	3.98	24 860
RT	3.25	22 763	RT	4.02	22 820
RT	3.28	20 219	RT	4.15	18 318
RT	3.31	21 853	RT	4.20	23 086
RT	3.36	23 557	RT	4.29	18 831
RT	3.40	23 112	RT	4.37	18 668
RT	3.54	24 201	RT	4.43	18 287

The probabilities $p_i(\lambda)$ are the squared component of the normalized relative displacements for each atom/direction i, $p_i(\lambda) = |\vec{\eta}_i(\lambda)|^2$, where $\vec{\eta}_i(\lambda) \propto M^{-\frac{1}{2}}\vec{e}_i(\lambda)$, and $\langle \eta_\lambda | \eta_\lambda \rangle = 1$. Note that we normalize $\eta(\lambda)$ for this purpose—ordinarily it is the eigenvector of the dynamical matrix, $\mathbf{e}(\lambda)$, that is normalized, not the displacement pattern. The participation number gives (roughly) the number of atoms that participate in the vibrational mode. A high participation number indicates a large number of atoms are involved and thus involves a global motion. A low participation number on the other hand indicates that very few atoms are displaced and the mode is localized.

The first four modes (table 1) are essentially transverse sound waves that propagate down the axis (z-axis) of the capsid shell, and are similar to waves on a string. The four modes are located at 1.45, 1.62, 1.74 and 1.88 cm^{-1}. Two of the modes (at 1.45 and 1.62 cm^{-1}) are cosine waves with transverse displacement patterns (one along x and the other along y). The next set of transverse waves (at 1.74 and 1.88 cm^{-1}) are sine waves also with perpendicular displacement patterns. Two of the wave patterns are illustrated on a single periodic unit of the M13 capsid in figure 4. Figure 4(a) shows the mode at 1.45 cm^{-1} and figure 4(b) shows the mode at 1.74 cm^{-1}. The arrows in the figures represent the center of mass motion of a single α-helix building block that is composed of 50 amino acids. The other two modes at 1.62 and 1.88 cm^{-1} are not shown since they have nearly identical displacement patterns as the modes at 1.45 and 1.74 cm^{-1} respectively, but along the perpendicular y-axis.

In an elastic continuum, these modes would be four-fold degenerate. However, since the capsid is composed of many α-helices arranged with helical symmetry about the z-axis, the displacements are *not* symmetric. For example, because the cosine wave is shifted by a phase factor the largest amplitudes occur on a different section of the α-helical building blocks compared with the sine waves. This produces the small splitting of the frequencies. It is interesting that a relatively simple calculation of the transverse speed of

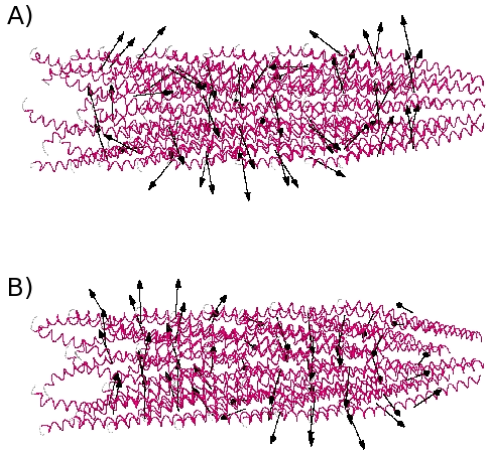

Figure 4. Transverse 'waves on a string' modes of one polarization (along x) for M13. (a) The mode at 1.45 cm^{-1} with cos (kz) dependence. (b) The mode at 1.74 cm^{-1} with sin (kz) dependence. Due to internal structure of the capsid, neither the x and y polarizations nor the sin and cosine wave forms are degenerate as in an elastic continuum theory.

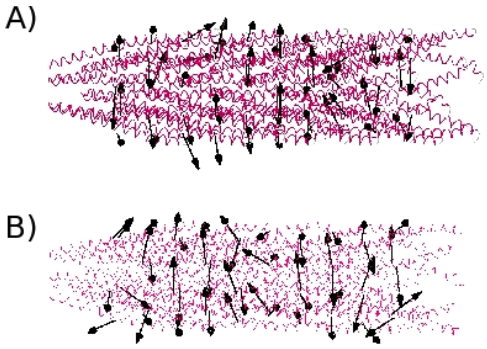

Figure 5. Torsional modes of the M13 capsid. (a) The mode at 2.67 cm^{-1} which has cos (kz) dependence. (b) The mode at 2.72 cm^{-1} with sin (kz) dependence. Due to the atomic structure of the capsid there is a small splitting of the frequency.

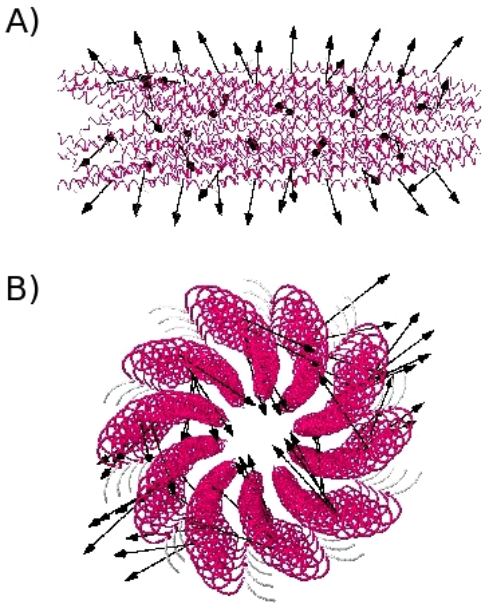

Figure 6. Compressional mode of the M13 capsid at 3.25 cm^{-1} viewed from two different locations. The displacements result in capsid compression along the x-axis and capsid expansion along the y-axis. (a) Looking down the x-axis at the top of the tube. (b) Looking down the z-axis of the tube.

sound in the capsid can be computed via $\omega = c_t k$ for the four different waves yielding values that range from $c_t = 702.5$ to 910.8 m s^{-1}. The last result is consistent with the speed of sound used in continuum model studies ($c_t = 915$ m s^{-1}) of the M13 phage [11, 20] taken from experiments on lysozyme [41]. The NMA with the atomistic structure however, provides an indication that a single value for the speed of sound in a nanoscale material may produce some inconsistencies.

The next highest frequency modes examined (illustrated in figures 5(a) and (b)) are a pair of torsional modes located at 2.67 and 2.72 cm^{-1}. These modes provide a twisting of the capsid (like the wringing of a dish cloth) about the z-axis of the capsid. The mode at 2.72 cm^{-1} is phase shifted from the 2.67 cm^{-1} mode by a factor of $\pi/2$ along the z-axis. These two modes produce a cos (kz) and sin (kz) dependence along the z-axis similar to that of the string modes. Again, there is a small splitting in the frequencies due to the atomic structure of the tube.

The next modes examined at 3.25, 3.28, 3.36, and 3.40 cm^{-1} can be best described as a transverse (to the tube axis) compressional squash of the capsid. The top view (looking down the x-axis) of the mode pattern at 3.25 cm^{-1} is illustrated in figure 6(a) and the view from down the axis of the tube (z-axis) is shown in (b). The transverse compression squeezes the capsid inward along the x-axis while the capsid expands outward along the y-axis. These modes are uniform down the z-axis i.e. they have no cos (kz) or sin (kz) dependence.

The last two mode patterns that we show are (i) a pair of axial modes (one of the pair is shown in figure 7(a)) located at 3.97 and 3.98 cm^{-1} and (ii) a breathing mode located at 5.22 cm^{-1} (figure 7(b)). The axial modes have a majority of their displacement along the z-axis of the capsid. The axial mode shown can be best described as a 'shearing' of the capsid along the z-axis which results in the top and bottom halves of the capsid moving in opposite directions. Looking down the z-axis of the tube, one would see one half of the capsid moving towards the viewer and the other half moving away. The breathing mode (figure 7(b)) has each α-helix building block moving approximately radially outward. Both modes (i) and (ii) are uniform down the z-axis of the capsid.

All of the modes shown above are also predicted in continuum theory [11]. The frequencies of the modes of the M13 capsid predicted with the continuum model and the atomistic model are compared in table 2. The few lowest frequencies and mode patterns predicted with continuum theory compare quite well with the atomistic predictions. But there are significant discrepancies. First, continuum theory predicts the next set of low frequency modes, after the breathing mode to be at around 10.0 cm^{-1}. The atomistic model predicts many more modes in the range of 3.0–

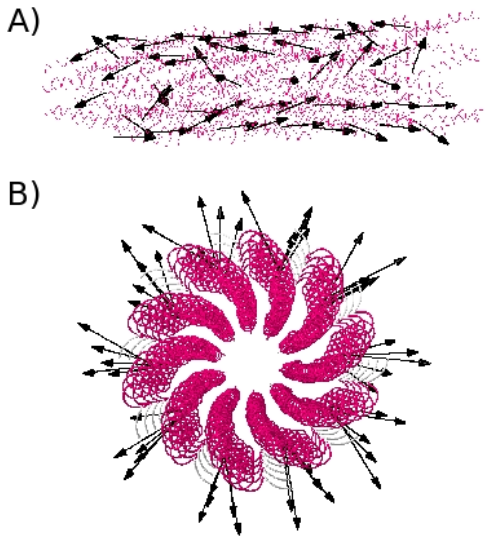

Figure 7. An axial mode and the breathing mode of the M13 capsid. (a) The axial mode of the M13 capsid at 3.97 cm^{-1}. The top half of the capsid shell moves in along the $-z$-axis while the bottom half moves along the $+z$-axis. (b) The radial breathing mode at 5.22 cm^{-1}. The displacements of each α-helix building block is approximately radially outward.

Table 2. Comparison of some of the frequencies predicted with a continuum elastic theory (CET) [11] and with an atomistic model (AM). Frequencies are listed in cm^{-1}. The corresponding figure showing the atomistic displacement pattern is also given.

CET	AM	Figure
1.22	3.25	6
1.85	3.97	7(a)
1.87	1.45	4
2.60	2.67	5
3.29	5.22	7(b)

10.0 cm^{-1}. Second, the displacement patterns have small fundamental differences. These differences may be important when predicting Raman spectra which depends directly on atomic displacements.

7. Raman spectral predictions for M13 phage

We now evaluate the Raman spectra of the M13 bacteriophage of an ensemble in solution using a simple empirical bond polarizability model for the quantum mechanical matrix elements of the polarizability derivatives that determine the Raman cross section. In solution, the viral particles will have a random orientation on average, and this is the case we consider here. Thus, one can derive [11] the average relative Raman intensity received by the detector (at polar angle Θ)

$$I_{\rm avg} \propto \frac{1}{2}\frac{\lambda_{\rm R}}{\omega}\left[{\rm Tr}(\Delta \overleftrightarrow{\chi})\right]^2 + \frac{\mu_{\rm R}}{\omega}{\rm Tr}\left(\left[\Delta \overleftrightarrow{\chi}\right]^2\right), \qquad (23)$$

where $\overleftrightarrow{\chi}$ is the 3×3 susceptibility tensor and $\lambda_{\rm R}$ and $\mu_{\rm R}$ are geometric factors, $\lambda_{\rm R} = [4-6\sin^2\Theta]$ and $\mu_{\rm R} = [14-\sin^2\Theta]$.

To calculate the change in susceptibility, we use the bond polarizability model [42–44] which calculates the total susceptibility as a sum over individual bond polarizabilities,

$$\Delta \overleftrightarrow{\chi} = \sum_{\rm bonds} \Delta \overleftrightarrow{\alpha}, \qquad (24)$$

where the change in the polarizability of single bond (between say atoms i and j) is

$$\Delta \overleftrightarrow{\alpha} = (\nabla_i \overleftrightarrow{\alpha}) \cdot \vec{\eta}_i + (\nabla_j \overleftrightarrow{\alpha}) \cdot \vec{\eta}_j. \qquad (25)$$

The del operator ∇_i denotes the gradient with respect to only atom i and $\vec{\eta}_i$ is the displacement vector for atom i, $|\eta\rangle = M^{-\frac{1}{2}}|e\rangle$. The polarizability tensor $\overleftrightarrow{\alpha}$ for a single bond can be written in terms of the projector operator

$$\overleftrightarrow{\alpha} = \alpha_{\parallel} \overleftrightarrow{P} + \alpha_{\perp}(\overleftrightarrow{I} - \overleftrightarrow{P}), \qquad (26)$$

where $\overleftrightarrow{P} = |\hat{d}\rangle\langle\hat{d}|$ and $\hat{d}$ is the unit direction vector for that bond.

In general, each bond will have a unique set of polarizability parameters that are required for the bond polarizability model. For the M13 phage capsid, we expect that the important contributions to the Raman intensity come from symmetry of the individual bond motions in the capsid due to a vibrational displacement and that differences in polarizability parameters of each bond have a smaller contribution. Thus as a first approximation we use a single set of parameters (from carbon–carbon bonds in C_{60} and C_{70} Raman spectra fits) for the model. Two choices can be made for the parameters and we examine the result from both.

The first set of parameters were obtained from Snoke and Cardona [42]. The parameters were obtained from fits to the Raman spectra of C_{60}. This resulted in fitted parameters for single bonds of $\alpha'_{\parallel} - \alpha'_{\perp} = 1.20$ Å^2, $2\alpha'_{\perp} + \alpha'_{\parallel} = 1.70$ Å^2, and $(\alpha_{\parallel} - \alpha_{\perp}) = 0.50$ Å^3. Similar parameters were also obtained by Guha *et al* [44] using vibrational eigenvectors calculated from first-principles. The static polarizability properties and the Raman scattering intensities in molecular C_{60} and C_{70} are found to be well reproduced by a bond polarizability model with parameters similar to those obtained from studies of hydrocarbons. For the Raman spectrum of C_{60} with off-resonance infrared laser excitation, a fit using first-principles vibrational eigenvectors yields $\alpha'_{\perp} - \alpha'_{\parallel} = 2.30$ Å^2 and $2\alpha'_{\perp} + \alpha'_{\parallel} = 2.30$ Å^2 for single bonds with $(\alpha_{\parallel} - \alpha_{\perp})$ arbitrarily set equal to its value in ethane, namely, 1.28 Å^3.

The displacement patterns from the fully atomistic NMA were used to construct the relative Raman intensity for the modes using equation (23) at a detector angle of $\Theta = 90°$. Figure 8 shows the relative Raman intensity of the modes between 0 and approximately 10 cm^{-1}. A broadening of 0.75 cm^{-1} was used. The Raman intensity using polarizability parameters from Snoke and Cardona is shown in figure 8 as the solid line. The dashed line is the Raman intensity when parameters from Guha *et al* are used. Both results give a single peak near 5.5 cm^{-1} and are remarkably similar.

For the purposes of comparison, we have also calculated a theoretical Raman profile for the M13 phage using continuum

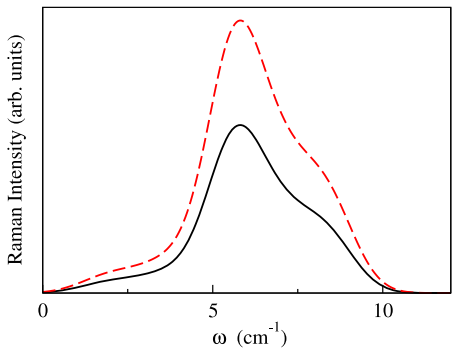

Figure 8. Relative Raman spectra predictions of the M13 capsid using displacement patterns from the atomistic model. Two curves are shown corresponding to different sets of polarizability parameters. The solid line was obtained using parameters from [42] and the dashed line from parameters in [44]. The results show predictions that are qualitatively independent of the parameter set chosen.

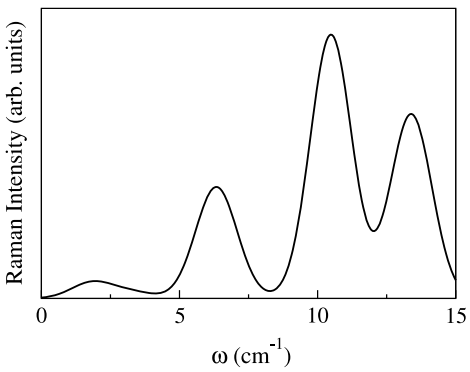

Figure 9. Relative Raman spectra predictions of the M13 capsid using displacement patterns from the continuum model. The calculation of the intensity profile follows the procedure in [11]. The contribution from all Raman active modes are shown.

elastic theory to predict the mode patterns. The susceptibility tensor required for the Raman predictions is calculated using an 'averaged' bond polarizability model (Amorphous Isotropic Bond Polarizability model) which was highlighted in our previous work [11]. Figure 9 shows *all* Raman active modes between 0 and 15.0 cm^{-1} that are predicted by continuum elastic theory. A broadening of 0.75 cm^{-1} was applied to each peak as in the atomistic case. In the continuum case three distinct peaks emerge compared with the single peak that results when atomistic modes are used. This is due to the large number of additional modes with small frequency difference (0.1 cm^{-1}) which combine to give a single broad peak in the atomistic model. Experimental low frequency Raman scattering measurements have been performed on the M13 phage and also show a single broad peak at approximately 8.5 cm^{-1} [45], in close agreement with the atomistic prediction. The likely conclusion that can be drawn is that many vibrational modes contribute to the Raman intensity. However, since the experiment was unable to resolve frequency differences less than 5.0 cm^{-1} due to inhomogeneous broadening, it is unclear if the experimental Raman profile was indeed the result of many modes or just a few.

8. Effects of water dampening

Viral capsids are present in a diverse medium of water, ions, and other molecules. Although the potential energy model used in the present work includes interactions with water in an average way, it does not incorporate dampening affects. Dampening due to the presence of water affects the vibrational frequencies of the capsid as well as the rate of decay of the vibrational amplitude. It is likely that some modes will be highly damped due to their tight coupling with the solvent, while others have only minor dampening. Dampening is an important effect as it will determine which modes are the most susceptible to being resonantly pumped and have significant lifetimes.

In previous work, dampening has been studied using continuum models [21, 46, 47] in which the viral capsid (treated as an elastic material) is embedded within a second elastic material with appropriate Lamé constants. In a continuum study of the M13 phage, Fonoberov *et al* [21] have performed this analysis. For the first couple of radial modes of M13, they obtain frequency shifts on the order of 0.3 cm^{-1}. The quality factors were 3.6–10 for the first couple of radial modes in M13. Thus the effects of dampening on tubular capsid appears to be significant, but the undamped modes offer a reasonable starting approximation of their dynamical properties. Dampening in spherical viruses have been studied by Murray *et al* [47] and Talati *et al* [46]. Murray performed a dimensionless analysis which gives a broad worldview of what is expected. The results depend of the radius of the virus, and the spherical harmonic ℓ value of the vibration. For a 50 nm diameter spherical virus, the imaginary part of the frequency (the dampening) is generally 5–20% of the oscillatory frequency. Higher angular momentum ℓ values give the largest dampening for the very lowest frequency modes.

Currently the phonon functional produces no estimates for the dampening produced by the surrounding solvent. A future direction of research is to incorporate dampening effects into the functional. A natural method to accomplish this is to use the method of Langevin modes [31]. Langevin dynamics includes a frictional interaction of the atoms of the molecule with the solvent. Such interactions can be estimated by viscous Stokes interactions of the atoms of the virus that are accessible to solvent. The mathematical problem of determining Langevin modes requires diagonalization of a $6N \times 6N$ non-symmetric Langevin matrix. This matrix has similarities to the $3N \times 3N$ symmetric dynamical matrix. The doubling of dimensionality occurs because both displacement and velocity become involved. If this future extension of the phonon function to Langevin modes is successful, the phonon functional method would provide atomic detail in describing solvent dampening effects.

9. Conclusions

We have presented a fully atomistic normal mode analysis of the M13 bacteriophage using a method originally designed for electronic structure theory. This method (the phonon functional method) can be used on large systems to determine the lowest frequency modes. The NMA of the M13 bacteriophage has shown that the flavor of the lowest frequency modes are similar to those predicted by continuum elastic theory, however, there are noticeable differences between the two. Continuum theory predicts the first few lowest frequency modes of the M13 capsid well, however it misses a significant portion of other low frequency modes that are captured with an atomistic structure. This will have consequences on the prediction of the relative Raman spectra as the continuum theory will miss the contribution from other low frequency modes.

Although a continuum theory can give reasonable predictions of the mode flavor and frequency of the first few lowest modes of the M13 capsid, an atomistic picture provides additional detail by providing (i) relative atomic motions, (ii) the splitting of frequencies due to asymmetry, and (iii) a more complete low frequency spectrum.

Finally, we note that while the phonon functional method has been used here to study the low frequency vibrational spectrum of the M13 phage, the method has broader applicability to other systems. One example is large proteins, where the dynamic motions of the molecule can often be described by a few low frequency normal modes [48], that can be thought of as 'generalized' coordinates. Thus the phonon functional method can provide a way to determine the normal modes of a variety of large systems with atomic detail.

Acknowledgments

We thank Professor K-T Tsen and Daryn Benson for many stimulating discussions.

Appendix. Dynamical matrix operator

In this appendix, we show how the calculation of the dynamical matrix operating on a vector can be computed without explicit storage of the entire matrix. The discussion is specific to the case of a fully atomistic empirical energy model of the form

$$V = \sum_{\text{bond}} k_b(d - d_{\text{eq}})^2 + \sum_{\text{ang}} k_\theta(\theta - \theta_{\text{eq}})^2 + \sum_{\text{dih}} \frac{v_n}{2}\left[1 + \cos(n\phi - \gamma)\right] + \frac{1}{2}\sum_{i,j}\left(\frac{q_i q_j}{\epsilon d} + \frac{A_{ij}}{d^{12}} - \frac{B_{ij}}{d^6}\right). \quad \text{(A.1)}$$

Since equation (A.1) is a sum of individual energy terms, the operation of the dynamical matrix on a general vector **u** can be calculated term by term, in the same fashion that the total force is accumulated during a molecular dynamics simulation. Thus, the dynamical matrix operation can be written in the form

$$u'_{i\alpha} = (\hat{D}\mathbf{u})_{i\alpha} = \sum_{j\beta} \frac{1}{\sqrt{m_i m_j}} \frac{\partial^2 V}{\partial r_{i\alpha}\, \partial r_{j\beta}} u_{j\beta} \quad \text{(A.2)}$$

where i, j label the atom number and $\alpha, \beta = x, y, z$. The second derivatives are calculated analytically each time the dynamical matrix operation is required so that only a few of the matrix elements need be stored in computer memory. Since the calculation of the force vector in a molecular dynamics simulation proceeds in a similar manner and each energy term only contributes to a few matrix elements, the rough computational cost of the dynamical matrix operating on a single vector is on the order of a single molecular dynamics step where each step is of order N in difficulty.

The ability to calculate the dynamical matrix operating on a vector in order N steps requires that a finite cutoff for the non-bonded interactions must be used. This presents no problem for the short ranged van der Waals interactions (r^{-6} and r^{-12} terms), the screened Coulomb interaction is not as accommodating. Caution must be taken with the Coulomb terms as it has a long range dependence. Tests with medium sized molecules such as ubiquitin (unpublished) show that the effect on frequencies and eigenvectors from varying the cutoff between 10 and 30 Å is relatively modest (<10% error).

As an example of how the dynamical matrix calculation proceeds, consider a single Coulomb term between atoms m and n. This single term contributes to 36 dynamical matrix elements (3 degrees of freedom times 2 atoms, squared). The second derivatives of the energy with respect to position are easily calculated in terms of first and second derivatives of the distance between the atoms d ($d = |\vec{r}_m - \vec{r}_n|$) as

$$\frac{\partial^2 V_c}{\partial r_{i\alpha}\, \partial r_{j\beta}} = \frac{\partial^2 V_c}{\partial d^2}\frac{\partial d}{\partial r_{i\alpha}}\frac{\partial d}{\partial r_{j\beta}} + \frac{\partial V_c}{\partial d}\frac{\partial^2 d}{\partial r_{i\alpha}\, \partial r_{j\beta}}. \quad \text{(A.3)}$$

The first and second derivatives of V_c with respect to d are trivial, $\frac{\partial^2 V_c}{\partial d^2} = +2\frac{q_m q_n}{\epsilon d^3}$, $\frac{\partial V_c}{\partial d} = -\frac{q_m q_n}{\epsilon d^2}$. The derivatives of d are given by $\frac{\partial^2 d}{\partial r_{i\alpha}\, \partial r_{j\beta}} = -\frac{\partial d}{\partial r_{i\alpha}}\frac{\partial d}{\partial r_{j\beta}} + \frac{\delta_{\alpha\beta}}{d}(\delta_{im} - \delta_{in})$ and $\frac{\partial d}{\partial r_{i\alpha}} = \frac{r_{m\alpha} - r_{n\alpha}}{d}(\delta_{im} - \delta_{in})$, where δ_{im} etc are Kronecker delta functions After the appropriate derivatives are calculated, the 36 dynamical matrix elements are temporarily formed and the appropriate components of vector **u** are multiplied by the matrix elements and their contribution to the vector **u**′ are added in according to equation (A.2). The dynamical matrix elements are then discarded and the procedure continues to the next Coulomb term and the rest of the energy terms. At the end, the vector **u**′ is the appropriate result of the dynamical matrix operating on a vector **u**, $\mathbf{u}' = \hat{D}\mathbf{u}$.

References

[1] Shenton W, Douglas T, Young M, Stubbs G and Mann S 1999 *Adv. Mater.* **11** 253
[2] Flynn C E, Lee S W, Peelle B R and Belcher A M 2003 *Acta Mater.* **51** 5867
[3] Mao C, Solis D J, Reiss B D, Kottmann S D, Sweeney R Y, Hayhurst A, Georgiou G, Iverson B and Belcher A M 2004 *Science* **303** 213
[4] Knez M, Bittner A M, Boes F, Wege C, Jeske H, Maiss E and Kern K 2003 *Nano Lett.* **3** 1079
[5] Knez M, Sumser M, Bittner A M, Wege C, Jeske H, Martin T P and Kern K 2004 *Adv. Funct. Mater.* **14** 116
[6] Khalil A S, Ferrer J M, Brau R R, Kottmann S T, Noren C J, Lang M J and Belcher A M 2007 *Proc. Natl Acad. Sci. USA* **104** 4892–7

[7] Babincova M, Sorivong P and Babinec P 2000 *Med. Hypotheses* **55** 450–1
[8] Tsen K T, Tsen S W D, Chang C L, Hung C F, Wu T C and Kiang J G 2007 *Virol. J.* **4** 50
[9] Tsen K T, Tsen S-W D, Sankey O F and Kiang J G 2007 *J. Phys.: Condens. Matter* **19** 472201
[10] Tsen KT, Tsen S-W D, Chang C-L, Hung C-F, Wu T-C and Kiang J G 2007 *J. Phys.: Condens. Matter* **19** 322102
[11] Dykeman E C, Sankey O F and Tsen K-T 2007 *Phys. Rev.* E **76** 011906
[12] Yan YX, Gambel E B Jr and Nelson K A 1985 *J. Chem. Phys.* **83** 5391–9
[13] Belnap D M *et al* 2000 *J. Virol.* **74** 1342–54
[14] Hewat E A, Neumann E and Blaas D 2002 *Mol. Cell* **10** 317–26
[15] Miller D W and Agard D A 1999 *J. Mol. Biol.* **286** 267–78
[16] Dykeman E C and Sankey O F 2008 *Phys. Rev. Lett.* **100** 028101
[17] Cornell W D, Cieplak P, Bayly C I, Gould I R, Merz K M Jr, Ferguson D M, Spellmeyer D C, Fox T, Caldwell J W and Kollman P A 1995 *J. Am. Chem. Soc.* **117** 5179–97
[18] Tsui V and Case D A 2001 *Biopolymers* **56** 275–91
[19] Bashford D and Case D A 2000 *Annu. Rev. Phys. Chem.* **51** 129–52
[20] Balandin A A and Fonoberov V A 2005 *J. Biomed. Nanotechnol.* **1** 90–5
[21] Fonoberov V A and Balandin A A 2004 *Phys. Status Solidi* b **241** R67–9
[22] Tirion M M 1996 *Phys. Rev. Lett.* **77** 1905–8
[23] Tama F and Brooks C L III 2005 *J. Mol. Biol.* **345** 299–314
[24] Tama F, Gadea F X, Marques O and Sanejouand Y H 2000 *Proteins: Struct., Funct. Genet.* **41** 1–7
[25] Tama F and Brooks C L III 2002 *J. Mol. Biol.* **318** 733–47
[26] Li G and Cui Q 2002 *Biophys. J.* **83** 2457–74
[27] Soejima K, Kurihara Y, Kamiya K and Umeyama H 1999 *FEBS Lett.* **463** 19–23
[28] Hayward S 2001 Normal mode analysis of biological molecules *Computational Biochemistry and Biophysics* ed O M Becker, A D MacKerrell Jr, B Roux and M Watanabe (New York: Dekker)
[29] Lanczos C 1988 *Applied Analysis* (New York: Dover) chapter 3
[30] Sankey O F, Drabold D A and Gibson A 1994 *Phys. Rev.* B **50** 1376–81
[31] Lamm G and Szabo A 1986 *J. Chem. Phys.* **85** 7334–48
[32] Ordejon P, Drabold D A, Martin R M and Grumbach M P 1995 *Phys. Rev.* B **51** 1456–76
[33] Mauri F, Galli G and Car R 1993 *Phys. Rev.* B **47** 9973
[34] Daw M S 1993 *Phys. Rev.* B **47** 10895
[35] Li X P, Nunes R W and Vanderbilt D 1993 *Phys. Rev.* B **47** 10891
[36] Press W H, Teukolsky S A, Vetterling W T and Flannery B P 1986 *Numerical Recipes* (Cambridge: Cambridge University Press) p 303
[37] Marvin D A, Welsh L C, Symmons M F, Scott W R P and Strauss S K 2006 *J. Mol. Biol.* **355** 294–309
[38] Hawkins G D, Cramer C J and Truhlar D G 1996 *J. Phys. Chem.* **100** 19824–39
[39] Dykeman E C and Sankey O F, unpublished
[40] Cui Q, Li G H, Ma J P and Karplus M 2004 *J. Mol. Biol.* **340** 345–72
[41] Tachibana M, Kojima K, Ikuyama R, Kobayashi Y and Ataka M 2000 *Chem. Phys. Lett.* **332** 259–64
[42] Go S, Bilz H and Cardona M 1975 *Phys. Rev. Lett.* **34** 580–3
[43] Snoke D W and Cardona M 1993 *Solid. State Commun.* **87** 121–6
[44] Guha S, Menéndez J, Page J B and Adams G B 1996 *Phys. Rev.* B **53** 13106–14
[45] Tsen K T, Dykeman E, Sankey O F, Lin N-T, Tsen S-W D and Kiang J G 2006 *Virol. J.* **3** 79
[46] Talati M and Jha P K 2006 *Phys. Rev.* E **73** 011901
[47] Murray D B and Saviot L 2007 *J. Phys.: Conf. Ser.* **92** 012036
[48] Tama F and Sanejouand Y-H 2001 *Protien Eng.* **14** 1